Detecting Coronal Holes for Solar Activity Modeling

Marios S. Pattichis[1], Venkatesh Jatla[1], Rachel A. Hock[2], Carl J. Henney[2], and Charles N. Arge[2].
[1] {pattichis,venkatesh.jatla}@gmail.com
image and video Processing and Communications Lab
Dept. of Electrical and Computer Engineering
University of New Mexico, United States.
[2]AFRL/RVBXS Space Vehicles Directorate, United States.

Abstract—Solar image analysis relies on the detection of coronal holes for predicting disruptions to earth's magnetic field. This paper introduces a level-set method for detecting coronal holes based on the processing of extreme ultra-violet images (EUVI) and magnetic images. For validating the approach, two independent manual annotations were combined to produce a set of 46 consensus maps. Overall, the level-set method produces significant improvements over the currently used approach. Future work needs to focus on validating the approach on larger datasets, the integration of more imaging modalities, and an analysis of inter-rater and intra-rater variability.

I. INTRODUCTION

Solar activity can cause significant disruptions to earth's magnetic field. The primary sources of the solar wind are coronal holes, and it is through the solar wind that coronal mass ejections (i.e., large eruptions of plasma and magnetic field on the Sun) or CMEs propagate and eventually impact and disrupt the earth's global magnetic field. Forecasting the arrival time of CMEs requires accurate specification of the background solar wind [1]. Early prediction of solar events therefore requires accurate physical model initialization based on a careful segmentation of coronal holes.

Coronal holes have certain physical characteristics that can help us detect them in solar images. First, they are supposed to be unipolar since they represent open magnetic lines. Thus, the detection procedure needs to ensure that the detected coronal holes are dominated by positive or negative polarity. Furthermore, the coronal holes cannot cross magnetic neutral lines that represent polarity boundaries. Second, coronal holes tend to be at a lower temperature and density and thus appear darker in extreme ultra-violet images (EUVI). Thus, the detection of coronal holes requires integrated processing of two different types of images.

The coronal hole detection problem is illustrated in Fig. 1. The goal is to use the physical characteristics of the EUVI and magnetic images to detect the coronal holes. The currently used method for coronal hole detection is described in [2] and is given in Fig. 1(d). This earlier method provides a careful integration of the requirements for unipolarity and darker appearance in EUVI images. The approach also implemented basic denoising methods that avoid the inclusion of smaller area coronal holes. While other approaches have

also been proposed, there is a lack of application of modern segmentation methods. Method validation includes overall visual comparison between manual segmentation from a single rater and the automated segmentation method.

(a) EUVI image (synoptic image). (b) Magnetic image (photomap image).

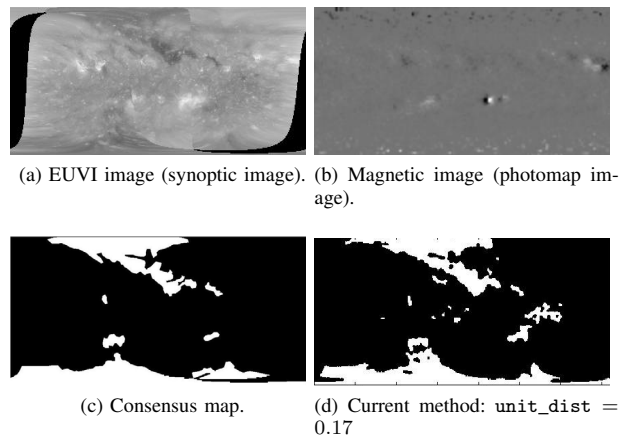(c) Consensus map. (d) Current method: `unit_dist` = 0.17

Fig. 1. The basic coronal hole detection problem. Example input data maps for May 2, 2011 are shown: EUVI (a) and magnetic image in (b). The consensus map for the coronal holes is shown in (c). Results from using the current method described in [2] can be found in (d). The `unit_dist` refers to the distance of the current algorithm from the ideal performance given by (`sensitivity`, `specificity`) = $(1, 1)$, where the ideal image is given in (c) (see (3)).

The current paper includes the following contributions over previously considered methods:

- *Segmentation using level-sets:* We introduce a new segmentation method by extending the level-set method presented in [3].
- *Method validation using consensus maps:* We validate our system using consensus maps derived from two independent raters.
- *Robust optimization using Pattern search:* We use a Pattern-search method to optimize the segmentation parameters. Here, we note that Pattern-search does not require derivatives and can deal with fairly noisy function evaluations [4].

The rest of the paper is organized as follows. In section

II, we provide a summary of the Henney-Harvey method for image segmentation. The Henney-Harvey method is used to initialize the new level-set segmentation method given in section III. Results are given in section IV. Concluding remarks are given in section V.

II. BACKGROUND

We summarize the Henney-Harvey method in Fig. 2. The algorithm takes the EUVI and magnetic (photomap) images as inputs and returns the segmented coronal hole image. The input images are resized to ensure that they share the same resolution.

An initial segmentation is estimated on the EUVI image. First, the dark regions in the EUVI images are detected using spatially adaptive thresholding (see Fig. 2). The need for adaptive thresholding comes from the fact that the EUVI images map the spherical surface of the sun to a rectangular image with pixels of variable size. These dark regions are denoised using a morphological `open-close`, followed by an area open that removes small blobs.

Magnetic constraints are then imposed on each estimated EUVI component based on the corresponding regions in the photomap (magnetic) image. To this end, the algorithm needs to determine the polarity of each EUVI component. An averaging filter is first applied to the polarity image to reduce the noise level. The polarity of each image is then computed as a ratio of the dominant polarity to the total number of pixels. The unipolar assumption is enforced by removing blobs for which the polarity ratio does not exceed 65%. The remaining blobs form the estimated coronal hole image.

III. METHOD

A. Manual annotation

To provide an independent validation, we use manual annotation. We manually segmented a set of 173 images by a trained undergraduate. The same set was then independently segmented by a second student (who was also trained). The two students were then brought together to provide consensus maps based on their independent segmentations. They completed 46 consensus maps (e.g., see [5]). We will report results on the consensus maps.

B. Level set segmentation

We develop a new segmentation method that is based on the Distance Regularized Level Set Evolution (DRLSE) method described in [3]. DRLSE defines:

$d_p(s) \triangleq p'(s)/s$ is a divergence operator,

$g = 1/(1 + |\nabla G * I|^2)$ is the edge function, and

$\delta_\epsilon(x)$ is zero for $|x| > \epsilon$ and non-zero for $|x| < \epsilon$

where $p(.)$ is used for defining a regularized distance for the level set function (ϕ), $g(.)$ should be minimized at image edges, ∇G denotes the gradient of the input image that is computed using convolution with a derivative of a Gaussian.

function HENNEYHARVEY(EUVI, mag)

▷ Threshold with area correction.
▷ θ comes from spherical coordinates.
▷ μ, σ are estimated over local windows.
$T \leftarrow \mu - \sigma(0.7 + 0.1\cos(\theta))$
`init_dark_img` $\leftarrow$ (EUVI $< T$)

▷ Reduce noise in EUVI image
`den_img` $\leftarrow$ **open-close** `init_dark_img` with SE
`den_img2` $\leftarrow$ **remove** small blobs from `den_img`
           with `area`< 25

▷ Denoise and prepare polarity image
`blurred`$\leftarrow$**blur** mag.
`pol_img`$\leftarrow$**compute_blob_polarity** of `blurred`

▷ Keep unipolar blobs only
`coronal_hole_img` $\leftarrow$ **remove** non-unipolar
           blobs from `den_img2`
           with $< 65\%$ in `pol_img`

return `coronal_hole_img`
end function

Fig. 2. Henney-Harvey method for detecting coronal holes.

The segmented image is computed by evolving the level set as given by:

$$\frac{\partial \phi}{\partial t} = \mu \mathcal{R}_p(\phi) + \lambda \mathcal{L}_g(\phi) + \alpha \mathcal{A}_g(\phi) \tag{1}$$

where:

$\mathcal{R}_p(\phi) = \text{div}(\text{d}_\text{p}(|\nabla\phi|)\nabla\phi)$ is the distance term,

$\mathcal{L}_g(\phi) = \delta_\epsilon(\phi)\text{div}(\text{g}\frac{\nabla\phi}{|\nabla\phi|})$,   is the boundary term, and

$\mathcal{A}_g(\phi) = g\delta_\epsilon(\phi)$ is an area term.

We provide a description of the proposed segmentation algorithm in Figs. 3 and 4. The approach requires joint processing of the EUVI and magnetic images. Most importantly, we need to modify the edge function so that it does not allow crossing the magnetic neutral lines. This is accomplished by modifying the edge function to be:

$$\text{pg} = (1 - \text{p})\text{g} \tag{2}$$

where p assumes the value of 1 over the magnetic polarity boundaries detected in the magnetic image and is zero away from the boundary (see Fig. 3). Thus, over the magnetic lines, the edge function becomes zero and prevents crossing of the neutral line boundary.

From (1), we have found that α and the spatial spread of the Gaussian (σ) used for computing the edge function are the two parameters that can affect overall segmentation performance. To find the optimal parameter values, we compare against the

```
function SEGMENT(EUVI, mag, α, σ)
    I ← smooth syn_img with 15 × 15 Gaussian kernel
            with optimization variable σ.
    g ← 1/(1+(I_x^2+I_y^2))

    ▷ Make g zero at magnetic boundaries
    p ← DetectMagneticCrossLines(mag_img)
    pg ← (1 - p ) .* g

    ▷ Initialize with HenneyHarvey segmentation method
    φ_0 ← HenneyHarvey (syn_img, photo_img)

    ▷ Run with modified edge function
    ▷ and optimization parameter α.
    return LS(EUVI, mag, φ_0, pg, α)
end function
```

Fig. 3. Main coronal hole segmentation algorithm. The parameters α and σ are optimized using `Pattern-Search`.

```
function LS(EUVI, mag, φ_0, pg, α)
    φ ← φ_0,      ▷ init. using previous method
    for i ≤ n do
        δ(φ) ← Dirac(φ, ε)

        ▷ Use modified edge function pg:
        F_a ← areaTerm(δ(φ), pg)
        F_e ← edgeTerm(δ(φ), φ, pg)
        F_d ← Regularize_distance(φ)

        ▷ Allow α to vary for optimization:
        φ ← φ + ts·(μF_d + λF_e + αF_a)
    end for
    return δ(φ)
end function
```

Fig. 4. Level-set segmentation algorithm using the modified edge function `pg` and α.

consensus maps, and look for the optimal values using (e.g., see [6]):

$$\min_{\alpha, \sigma} \sqrt{[1 - \text{spec}(\alpha, \sigma)]^2 + [1 - \text{sens}(\alpha, \sigma)]^2} \qquad (3)$$

where `Spec` denotes the (pixel-level) specificity and `Sens` denotes the corresponding sensitivity. The solution of (3) gives the optimal values for each image. For each image, we constrain the optimization problem for $\alpha \in [-3, +3]$, $\sigma \in [0.2, 1]$. Over the training set, we select the median values over the entire set. We then report the performance over the testing set. In the results section, we report the performance of the algorithm using leave-one-out.

The optimization of (3) is challenging since derivative estimates can be very noisy. To this end, we use a robust optimization method based on `Pattern-search` initialized with $\alpha_0 = 0, \sigma_0 = 0.5$. We refer to [4] for details on the optimization procedure. Furthermore, to speed-up convergence, we initialize the segmentation algorithm using the Henney-Harvey algorithm as documented in Fig. 3.

IV. RESULTS

We present results for the consensus maps ($N = 46$) in Table I. On average, we have a reduction of 19% ($\sigma = 17.7\%$) in the unit-distance from the ideal segmentation. On the other hand, we also have cases where the new method performs worse than the original `Henney-Harvey` method. We provide three representative examples in Figs. 5, 6, and 7.

The best case scenario is shown in Fig. 5. Here, it is clear that the level-set method provides smoother boundaries with coronal hole estimates that are better filled and in better agreement with the `Henney-Harvey` method. On the other hand, there are significant gaps in the original method.

Similar comments apply for the typical case shown in Fig. 6. Overall, a larger number of coronal holes appear in the original method that cannot be found in the consensus map. On the other hand, most of the smaller coronal holes are missing from the level-set approach.

For both methods, the worst case is shown in Fig. 7. In this example, both methods fail to fully detect the coronal hole in the north pole region. A careful examination of the EUVI image of Fig. 7(a) shows that the pixels in this north-pole coronal hole are much brighter than average. Thus, the initialization by the `Henney-Harvey` method fails to detect the coronal hole in the south pole and the level-set evolution does not recover from this initialization. Furthermore, the consensus map appears to have finer resolution detail than both maps. In this case, the level-set approach overly smooths the detected components as compared to the consensus map and the original method.
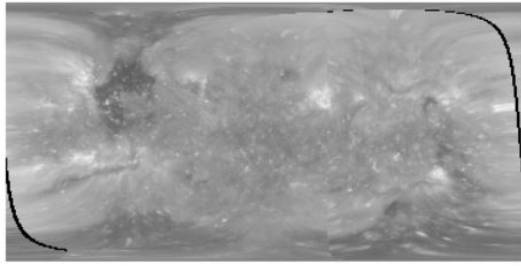
TABLE I
PERCENTAGE IMPROVEMENT OF PROPOSED LEVEL-SET SEGMENTATION METHOD (SEE (3) FOR DEFINITION OF UNIT DISTANCE). OVERALL, WE HAVE AN AVERAGE (MEAN) IMPROVEMENT OF **19.01**% WITH A STANDARD DEVIATION OF **17.7**%

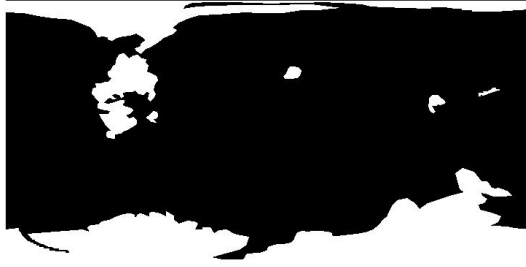| Order Stat.	Henney-Harvey	Level Sets	% Impr.
Min	0.14	0.17	-24.96
25%	0.26	0.27	-2.00
50%	0.31	0.27	12.06
75%	0.23	0.16	30.44
Max	0.19	0.09	50.76

V. CONCLUSION

The paper introduces the use of consensus maps for validating coronal hole detection methods. A level-set segmentation method is developed and compared against the currently used method for coronal hole detection. Overall, the proposed level-set approach provides significant improvements over the original method. On the other hand, we still have significant challenges for both methods, and we still have cases that level-sets under-perform the original method.
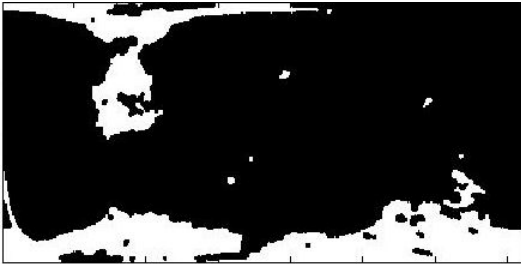
Future work should include studies on both inter-rater and intra-rater variability and how they are reflected in the
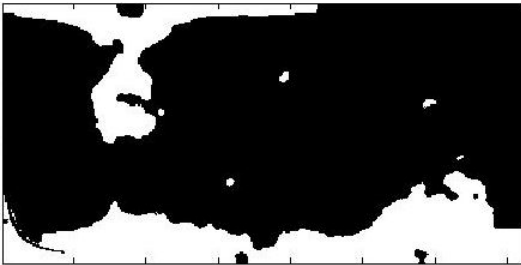
(a) EUVI

(b) Consensus map
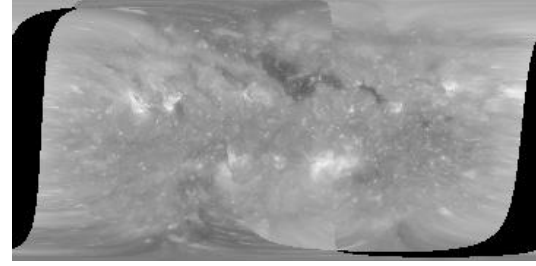

(c) `Henney-Harvey` Method, `unit_dist` $= 0.19$

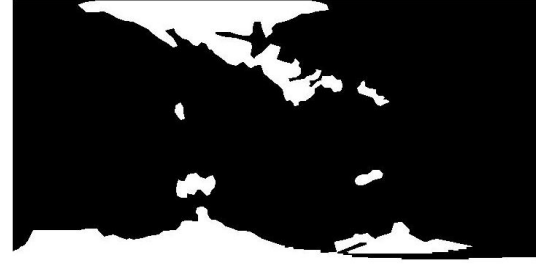(d) Level-set segmentation, `unit_dist` $= 0.09$

Fig. 5. Best case results for the level-set segmentation method for the input data from January, 24th, 2011. We have a reduction in the unit distance by 50.76% (see (3) for definition of unit distance).

(a) EUVI

(b) Consensus map

(c) `Henney-Harvey` Method, `unit_dist` $= 0.17$

(d) Level set segmentation, `unit_dist` $= 0.12$

Fig. 6. Typical case results for the level-set segmentation method for the input data from May 2, 2011. We have a reduction in the unit distance by 29.36% (see (3) for definition of unit distance).

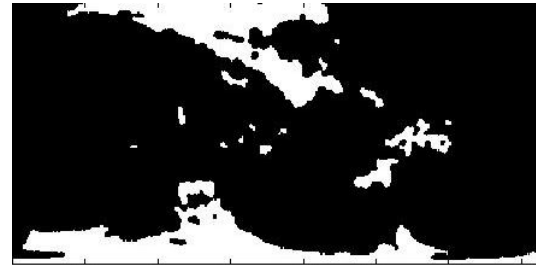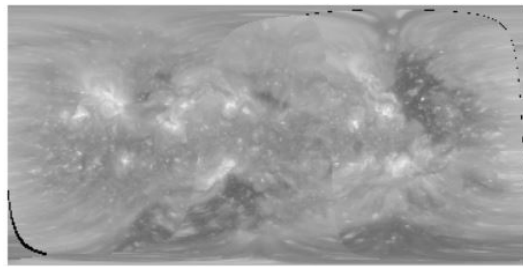consensus maps. We refer to [5] for a similar study using medical images.

Coronal hole segmentation method require significant improvements. Coronal holes at the poles should not be missed due to EUVI image intensity variations. Validation on larger datasets will most likely expose more issues. Segmentation performance can benefit by extending the methods to include more modalities as discussed in data fusion approaches (e.g., see [7]).

REFERENCES

[1] C. Lee, C. Arge, D. Odstrčil, G. Millward, V. Pizzo, J. Quinn, and C. Henney, "Ensemble modeling of cme propagation," *Solar Physics*, vol. 285, no. 1-2, pp. 349–368, 2013.
[2] C. Henney and J. Harvey, "Automated coronal hole detection using he i 1083 nm spectroheliograms and photospheric magnetograms," in *ASP Conf.*, vol. 346, 2005, pp. 261–268.
[3] C. Li, C. Xu, C. Gui, and M. Fox, "Distance regularized level set evolution and its application to image segmentation," *IEEE Transactions on Image Processing*, vol. 19, no. 12, pp. 3243–3254, Dec 2010.

(a) EUVI

(b) Consensus map

(c) `Henney-Harvey` method, `unit_dist` $= 0.14$

(d) Level set segmentation, `unit_dist` $= 0.17$

Fig. 7. Worst case results for the level-set segmentation method for the input data from February 29, 2011. In this case, we have an increase in the unit distance by 24.96% (see (3) for definition of unit distance).

[4] J. Nocedal and S. J. Wright, *Numerical Optimization*, 2nd ed. Springer, 2006.

[5] M. Pattichis, P. Soliz, and T. Cacoullos, "New models for region of interest reader classification analysis in chest radiographs," *Pattern Recognition, Special Issue of Digital Image Processing and Pattern Recognition Techniques for Detection of Cancer*, vol. 42, no. 6, pp. 1058–1066, 2009.

[6] C. Agurto, V. Murray, H. Yu, J. Wigdahl, M. Pattichis, S. Nemeth, S. Barriga, and P. Soliz, "A multiscale optimization approach to detect exudates in the macula," *IEEE Journal of Biomedical and Health Informatics*, 2014.

[7] C. S. Pattichis, M. S. Pattichis, and E. Micheli-Tzanakou, "Medical imaging fusion applications: An overview," in *Thirty-Fifth Asilomar Conference on Signals, Systems and Computers*, vol. 2, 2001, pp. 1263 – 1267.